



Article

Quantitative Study on Salinity Estimation of Salt-Affected Soils by Combining Different Types of Crack Characteristics Using Ground-Based Remote Sensing Observation

Zhuopeng Zhang ¹, Xiaojie Li ² , Shuang Zhou ¹, Yue Zhao ¹ and Jianhua Ren ^{1,*}

- ¹ Heilongjiang Province Key Laboratory of Geographical Environment Monitoring and Spatial Information Service in Cold Regions, Harbin Normal University, Harbin 150025, China; zhuopeng06@stu.hrbnu.edu.cn (Z.Z.); zhoushuang@stu.hrbnu.edu.cn (S.Z.); zhaoyue@stu.hrbnu.edu.cn (Y.Z.)
- ² Northeast Institute of Geography and Agroecology, Chinese Academy of Sciences, Changchun 130102, China; lixiaojie@iga.ac.cn
- * Correspondence: renjianhua@hrbnu.edu.cn; Tel.: +86-431-8554-2227

Abstract: Soil salinity is one of the parameters used for determining the extent of soil salinization. During water evaporation, the surface of salt-affected soils in the Songnen Plain, China, exhibits obvious shrinkage and cracking phenomena due to the high salt content. The aim of this current study is to quantify the influence of the salt content on the surface shrinkage–cracking process and to achieve quantitative extraction of soil salinity parameters based on different crack parameter types. In order to achieve the above objectives, a controlled shrinkage–cracking experiment was conducted. Subsequently, three kinds of crack characteristics such as crack length, box-counting dimension, and 12 gray-level co-occurrence matrix (GLCM) texture features were quantitatively extracted from the standard binary crack patterns. In order to predict the soil physical–chemical properties of salt-affected soils in the Songnen Plain, three models such as multiple linear regression (MLR), multiple stepwise regression (MSR), and artificial neural network (ANN) were developed and compared based on the crack length, box-counting dimension, and the first two principal components of GLCM texture features. The results show that the extent of desiccation cracks was determined by soil salinity since the water film caused by exchangeable cations and the thickness of DDL determined by soil salinity can promote desiccation cracking. Although the three methods have high prediction accuracy for Na⁺, electrical conductivity (EC), and total soil salinity, the ANN-based method showed the best prediction with R² values for Na⁺, EC, and soil salinity as high as 0.91, 0.91, and 0.89, and ratio of performance to deviation (RPD) values for Na⁺, EC, and soil salinity corresponding to 2.96, 3.47, and 2.95.

Keywords: salt-affected soil; soil salinization; Songnen Plain; artificial neural network; desiccation crack



Citation: Zhang, Z.; Li, X.; Zhou, S.; Zhao, Y.; Ren, J. Quantitative Study on Salinity Estimation of Salt-Affected Soils by Combining Different Types of Crack Characteristics Using Ground-Based Remote Sensing Observation. *Remote Sens.* **2023**, *15*, 3249. <https://doi.org/10.3390/rs15133249>

Academic Editor: Elias Symeonakis

Received: 13 April 2023

Revised: 20 June 2023

Accepted: 21 June 2023

Published: 23 June 2023



Copyright: © 2023 by the authors. Licensee MDPI, Basel, Switzerland. This article is an open access article distributed under the terms and conditions of the Creative Commons Attribution (CC BY) license (<https://creativecommons.org/licenses/by/4.0/>).

1. Introduction

In both arid and semi-arid areas, soil salinization is considered as very severe land degradation, which causes a great reduction in crop yields, damages the properties of the soil, and also poses a very large detrimental impact on the ecological environment. Therefore, determining the extent of salinization and measuring soil salinity quickly and accurately are important prerequisites for the scientific management and rational utilization of salt-affected regions [1]. In soil salinity detection methods, field sampling followed by traditional laboratory analysis is the most direct method [2,3]. However, real-time soil salinity parameters cannot be obtained effectively by conventional methods due to their tedious testing processes, long-term measurement periods, and high labor cost. The electromagnetic induction method is commonly used to determine the salt content without contact, which refers to a quick determination of the apparent soil conductivity by measuring the correlation between the primary magnetic field and the induced secondary magnetic

field [4,5]. Although this method is widely used when field monitoring the content and spatial distribution of soil salinity, soil texture measurement, and other soil properties [6–8], the accuracy of electromagnetic induction sensors such as the EM-38 can be easily affected by soil physical–chemical properties due to their high sensitivity. Moreover, the limitation of electromagnetic sensors also lies in their susceptibility to environmental influences [9–11]. Owing to its powerful data synthesis and high effectiveness, remote sensing technology is widely used to monitor soil salinity in large-scale and multi-temporal ways, which depends on the diagnostic spectroscopy of different salt minerals [12,13]. Many scholars have identified and classified saline–alkali soils using spectral measurements and the response of saline soils [14–17], band combinations of soil spectral features [18–20], and inversion modeling for soil salinity from different scales [21–23]. However, there are still many factors influencing the transmission process of electromagnetic waves, indicating that the estimation of soil salinity parameters using spectroscopy is often limited to qualitative descriptions [24–26]. Therefore, it is important and urgent to develop a quick and effective method to measure salinity levels without damaging the surface of salt-affected soil.

Due to its high clay contents, cohesive saline–alkali soil tends to generate desiccation cracks on its surface under drought conditions, which will weaken the mechanical properties of the soil and reduce the stability of the soil structure [27,28]. Therefore, quantifying the relationship between soil salinity and crack characteristics can greatly help to improve the accuracy in identifying the salinity of saline–alkali soils. In an earlier study, Lima et al. [29] confirmed that as the salt content increases, the area and volume of soil cracks increase, while the crack width showed an opposite trend. With the rapid development of the computer field, the accurate and effective acquisition of soil crack characteristics based on image processing technology has gradually attracted the attention of scholars, which makes more and more researchers strive to the influence of salinity on surface desiccation cracking of saline–alkali soils. Sun et al. [30] quantitatively analyzed changes in crack morphology by deploying saturated mud samples with different salt concentrations. Their results showed that the total crack length and the average crack width gradually decreased, and the cracking time of the soil surface was also delayed with salt concentration. Chang et al. [31] simulated the soil shrinkage characteristic curve using a trilinear model. They found that different concentrations of sodium salt solutions can destroy soil colloids, which in turn leads to soil shrinkage. DeCarlo et al. [32] proposed an X-ray microtomography method to determine the 3D crack parameters of mixed bentonite with different NaCl concentrations. They found that the soil cracks showed a concentrated distribution with the increase in soil salinity. Xing et al. [33] analyzed the effects of salt cations on the water-holding capacity and dry shrinkage cracking in pink clay loam soil in Shanxi, China. They found that four ions (Na^+ , K^+ , Mg^{2+} , and Ca^{2+}) can decrease the cracking degree of the soil, which thus provided a reference for the development of irrigation patterns for saline soils. After simulating the process of the dry cracking of laterite soil fractures, Huang et al. [34] found that the fractal dimension computed from the crack pattern was clearly positively correlated with the total crack length, the crack area, the crack rate, the crack node number, and the crack bar number, their results also indicated that the fractal dimension was significantly negatively correlated with the block area. Although many scholars have focused on the impact mechanism of soil salinity on the cracking process of salt-affected soils, the relationship between cracks and salinity still varies due to different conditions such as climate, topography, hydrological characteristics, and soil types. This is because the complex interaction between salt and soil particles during the desiccation cracking process is influenced by the valence state and the ion concentration, denoting that the mechanism by which the soil salt content affects the surface cracking of cohesive soil has not been fully determined.

Although many studies have focused on the characterization of desiccation cracking in relation to soil salinity, most of them rely on only one type of crack characteristics, which represents a limitation in describing the occurrence and development of cracks and also makes it difficult to fully quantify the effect of soil salinity parameters on the

desiccation cracking process. This study intended to explore the response of different crack characteristics to the soil salinity of salt-affected soils in the Songnen Plain of China. To achieve the objectives, a laboratory-controlled cracking test was designed using 57 soil samples. An attempt was also made to synthetically extract crack parameters, such as geometric, fractal dimension, and texture features based on the images obtained from ground-based remote sensing techniques, and to analyze the mechanism of soil salinity on the desiccation cracking process of cohesive salt-affected soils. After that, three different regression models were further developed and compared in order to estimate the soil salinity parameters effectively and accurately, which can thus provide accurate data support for the improvement of local salt-affected soils and can also be used to explore the possibility for further non-destructive and online measurement of soil salinity under field conditions at different scales.

2. Materials and Methods

2.1. Study Area

The Songnen Plain is commonly considered one of three typical soda-salt-affected soil concentration areas worldwide. With the increase in human activities and the imbalance between resource utilization and environmental protection, the soil salinization of the Songnen Plain is showing a trend of increasing year by year. The cohesive soil in the area suffers from soil salinization and is almost completely scattered with very low soil permeability, leading to significant shrinkage and cracking on the soil surface during the evaporation of water, which severely restricts the sustainable development of both livestock and agriculture in the region. Figure 1 describes the surface desiccation cracks developed from typical soda salt-affected soil with different salt contents in the Songnen Plain under natural conditions.

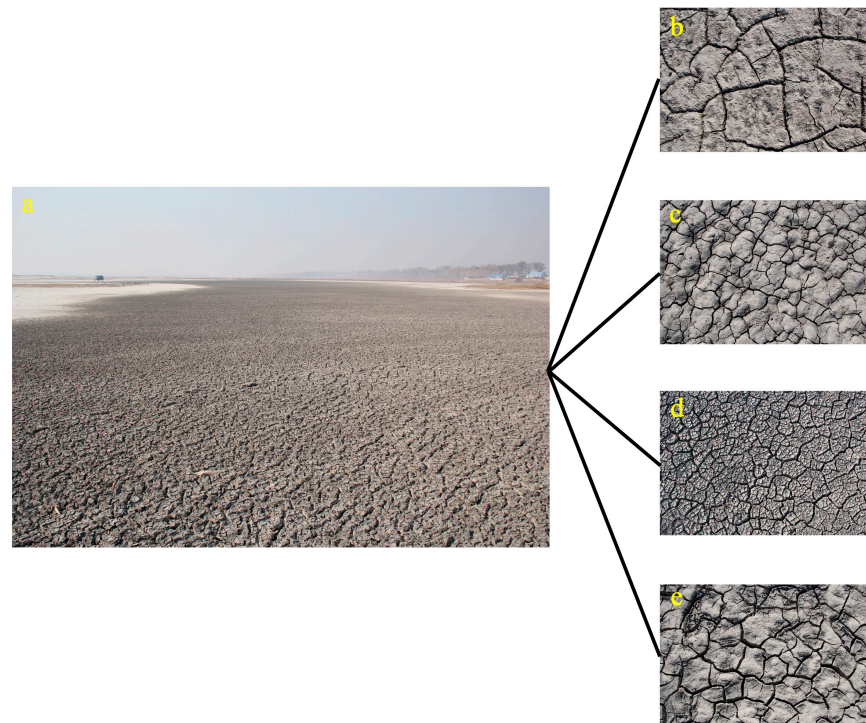


Figure 1. Desiccation cracks generated on the surface of salt-affected soil. (a) Overall cracking conditions at 123°52'46''E, 45°36'36''N, (b) cracking surface at 123°47'59''E, 45°26'16''N, (c) cracking surface at 123°44'27''E, 45°37'57''N, (d) cracking surface at 123°56'30''E, 45°23'58''N, (e) cracking surface at 124°3'33''E, 45°32'28''N.

In this study, Da'an City was determined as the main research area, which is located in the western region of the Songnen Plain. The annual average temperature in Da'an City is 4.5 °C with annual minimum and maximum temperatures of −35 °C and 36.9 °C, respectively. In addition, the rainfall in this area is concentrated in July and August, with annual average evaporation of up to 1900 mm; however, the annual average precipitation is only maintained at approximately 400 mm. This seriously unbalanced evaporation–precipitation ratio, coupled with the impact of local special terrain, hydrogeological conditions, and unreasonable anthropogenic activities such as flood irrigation, excessive deforestation, over-cultivation, and overgrazing have made the study area one of the most severely salinized regions in the Songnen Plain [35]. The primary salt minerals of salt-affected soils in Da'an City are NaHCO₃ and Na₂CO₃. This kind of salt-affected soil with low infiltration capacity can largely prevent salt from moving downward, denoting that the soil properties are thus stable from the topsoil layer. Therefore, after consideration of the environmental factors and spatial heterogeneity, 57 soil samples were obtained from the top 20 cm with the sampling points distributed in Figure 2. Note that all soil samples were selected within a small region with longitude from 123°42'33"E to 124°6'1"E and latitude from 42°23'57"N to 45°39'57"N. After air-drying, grinding, and sieving all soil samples through a 2 mm mesh, they were divided into three parts: the first sub-samples were used for determining the soil chemical parameters, the second sub-samples were prepared for measuring the soil particle size distribution, and the third sub-samples were used to simulate a shrinkage–cracking test on the soil surface.

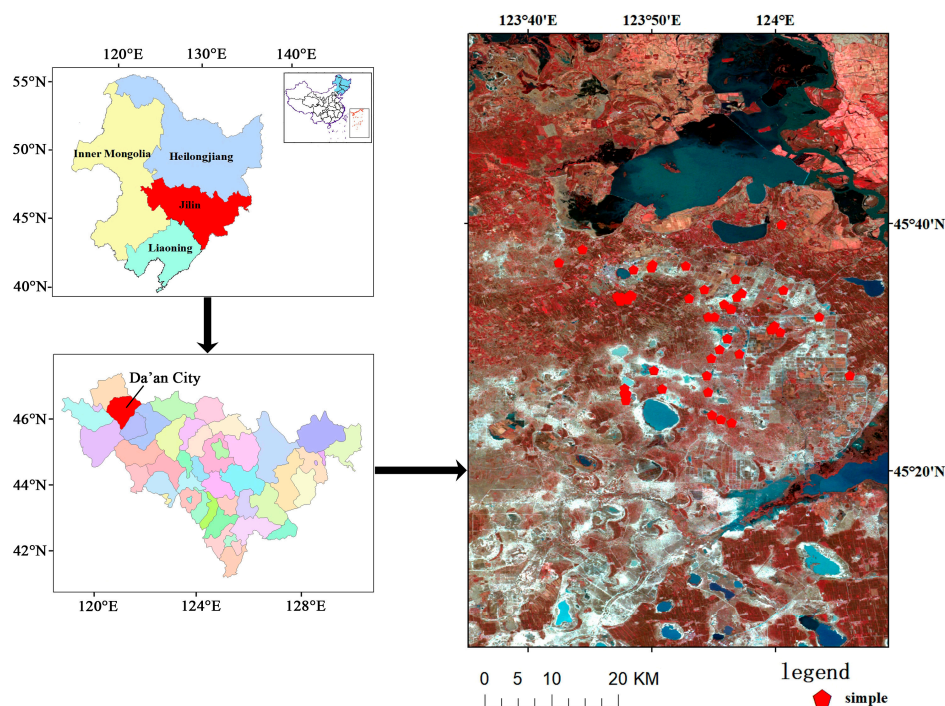


Figure 2. Study area and soil sampling distributions.

2.2. Soil Property Measurements

In this study, salinity parameters refer to pH, electrical conductivity (EC), sodium adsorption ratio (SAR), exchangeable sodium saturation percentage (ESP), and the eight main ions of salt-affected soil, including Na⁺, K⁺, Mg²⁺, Ca²⁺, Cl[−], HCO₃[−], CO₃^{2−}, and SO₄^{2−}. Note that since the saline-sodic soils of the Songnen Plain are almost devoid of SO₄^{2−} [36,37], the measurement of SO₄^{2−} was therefore neglected in the present study. After preparing soil suspensions with a soil–water mass ratio of 1:5, the EC values and pH of soil samples were measured based on the conductometric method and the potentiometric method, respectively. After that, a soil extract with the same soil–water mass ratio was

used to determine the ion contents of all soil samples. Specifically, a flame photometer was used for the contents of Na^+ and K^+ ; the EDTA titration method was carried out for the contents of Mg^{2+} and Ca^{2+} ; the AgNO_3 solution titration method was used to measure the content of Cl^- ; and the HCO_3^- and CO_3^{2-} contents were determined based on the double indicator neutralization method. In addition, a Millvern MS-200 laser particle size analyzer was used for the particle size distribution of all the soil samples.

2.3. Soil Surface Cracking Experiments

To simulate the shrinkage and cracking process, 57 saturated slurry samples with the same water content of 80% were prepared, mixed, stirred well, and poured into square wooden sample boxes of the same size ($50 \times 50 \times 3$ cm) and the surface was smoothed using a spatula. After that, the prepared soil samples were then placed and dried under controlled laboratory conditions with temperature, humidity, and pressure kept at 25°C , 35%, and 101 kPa, respectively. After each soil sample was weighed every day, a standard process was used to take photos of the cracking status of all soil samples. In particular, a digital camera with high resolution was first fixed on an experimental metal platform to take standard images of all soil samples during the desiccation cracking process, ensuring that the lens was pointed vertically down and at a height of 1 m from the ground. Second, a fixed area of $50 \text{ cm} \times 50 \text{ cm}$ was determined, with the center corresponding to the projection of the camera lens on the ground. Third, the light sensitivity of the laboratory was measured using a digital photometer. After that, the white balance process of the camera was carried out accordingly; in addition, some other camera parameters including shutter speed and aperture size were also configured and set. Thereafter, every soil sample was then placed in a fixed area above and photographed for a standard crack pattern of the same size. After the images of all cracked soil samples were obtained every day, a black-and-white grid calibration plate (size of $50 \text{ cm} \times 50 \text{ cm}$) was covered on the fixed area mentioned above and photographed again for further geometric calibration. Figure 3 shows the desiccation cracking process of a typical soil sample in this study. When the mass of all samples no longer decreased, the cracking process could be considered finished, and the soil samples were thus considered completely dried soil samples.

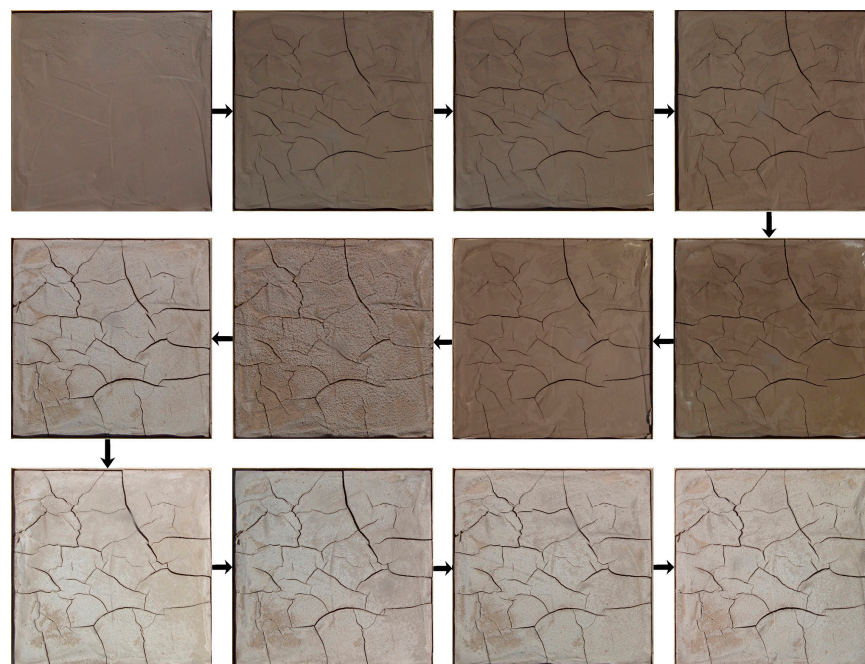


Figure 3. Cracking process of a typical soil sample in this study.

2.4. Standardized Preprocessing of Crack Images

After the drying process was fully completed, polynomial-based geometric distortion correction was applied to all crack patterns based on the grids of the calibration plate. In order to avoid the influence of shadows generated from the edges of frames, all corrected images were cropped using a uniform size of 47.5 cm \times 47.5 cm. To accurately extract various kinds of crack characteristics, all standard crack images were subjected to a standard preprocessing operation, as shown in Figure 4.

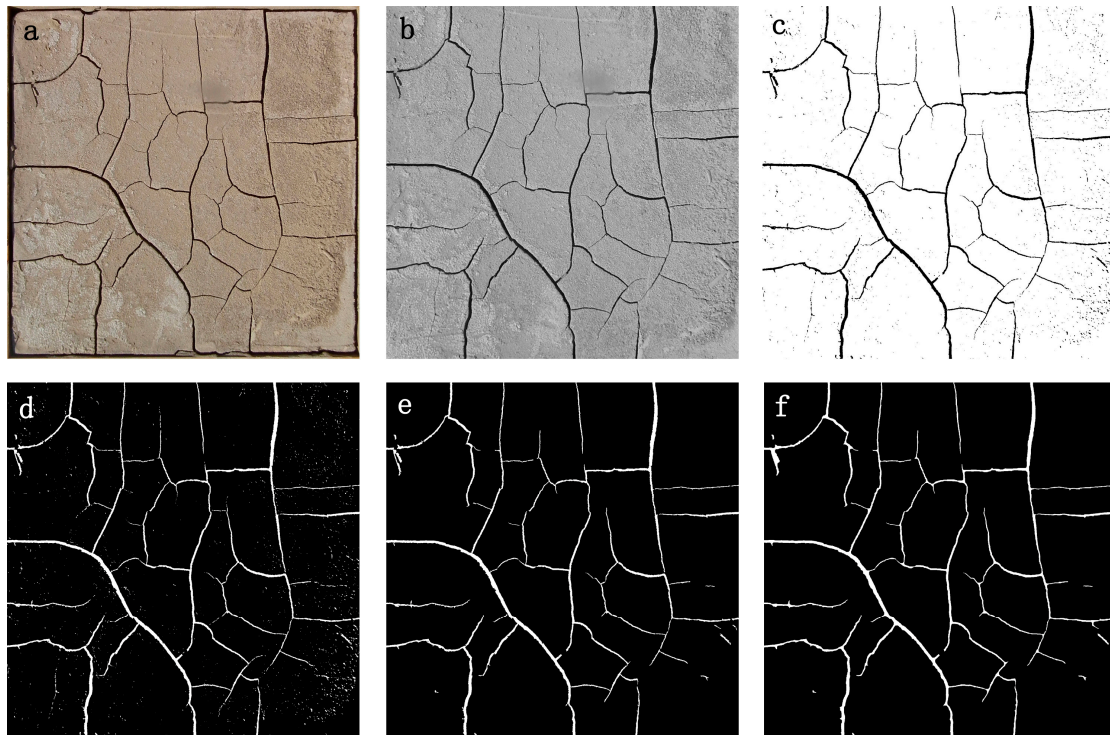


Figure 4. Standardized preprocessing process for crack images. (a) Crack image after geometric correction, (b) grayscale crack image, (c) binarized crack image, (d) inversed binary image, (e) denoised crack image, (f) crack image after bridging process.

First, the red, green, and blue components of each crack image (Figure 4a) were averaged for a grayscale image (Figure 4b). Second, a grayscale threshold was determined for each crack image based on the statistical histogram of the gray levels and then used to perform binarization for all grayscale images (Figure 4c). The binarized images were then inverted to highlight the cracked areas and facilitate subsequent crack feature extraction (Figure 4d), where the white areas represent the cracked regions and the black areas signify the uncracked soil surface. Fourth, an open-operating process with a given threshold (50 pixels was chosen for this study) was performed to remove noise because of small amounts of soil weeds and salt that precipitated on the soil surface during the drying process (Figure 4e). Finally, a given threshold of 10 pixels to perform expansion operation was carried out to eliminate the narrow space between cracks with a distance of fewer than 10 pixels and achieve the bridging processing of crack fracture parts (Figure 4f).

Figure 5 shows the crack images of all 57 soil samples obtained based on the standardized preprocessing according to the operation mentioned above.

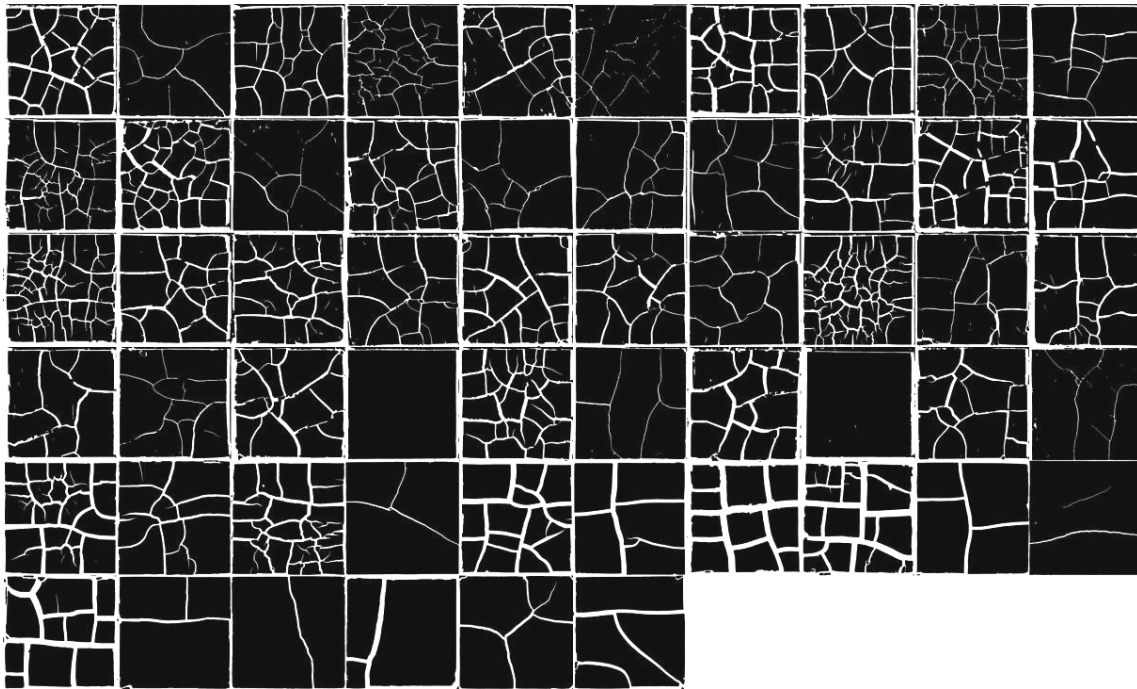


Figure 5. Binarization preprocessing results of all soil samples.

2.5. Crack Feature Extraction

2.5.1. Crack Length

Crack length (CL) is one of the most commonly used geometric features to quantify the extent of desiccation cracking generated on the soil surface, which also allows the visual determination of desiccation crack development. To extract the crack length of the cracked samples accurately, a skeletonization algorithm was used in this study to repeatedly remove pixels from the boundary of the crack region of the binary crack images until the width of the skeleton reached one pixel. Subsequently, a threshold of 10 pixels was set to remove extra burrs generated from the skeletonization process. Following the processes described above, the number of pixels in the skeleton was extracted from each crack pattern to compute the crack length according to the actual size of one pixel in the standard crack image.

2.5.2. Fractal Dimension

Fractal theory is often introduced to represent various irregular phenomena and objects in nature, which also helps explain complex and nonlinear problems. The process of desiccation cracking is very random in nature, showing that the fractal dimension can thus be extracted to quantify the cracks generated on the soil surface. In this study, the well-known box-counting dimension (D) was selected as the main method to describe the fractal dimension of desiccation cracks [38]. In particular, the box-counting dimension focuses on computing the number of boxes covering the object to evaluate the coverage of irregular collections, which was calculated using the following equation:

$$D = \lim_{\delta \rightarrow 0} \frac{\ln N(\delta)}{\ln(\frac{1}{\delta})} \quad (1)$$

where δ describes the width of the square box covering the cracked image at a specific equal-partition condition (two equal partitions were selected in this study), and $N(\delta)$ refers to the number of non-empty boxes corresponding to a given box width δ . Note that since δ cannot converge to zero indefinitely, the box-counting dimension is thus represented and

estimated by extracting the slope value of the linear equations corresponding to δ and $N(\delta)$ in the double logarithmic coordinate system in the actual calculations.

2.5.3. Texture Feature

Texture features usually represent visual features that are not determined by the brightness or color of an image and can thus describe the homogeneous phenomenon of the image, which also reflects the image element distributions of the neighborhood space [39–41]. In all types of texture analysis, the gray-level co-occurrence matrix (GLCM) is usually considered the most representative method, which can be extracted by computing the conditional probability density of the second-order combinations between different gray levels of pixels within the image [42,43]. GLCM textures can be introduced to characterize the variations and structure of desiccation cracks generated on salt-affected soils since the development and expansion of cracks are statistically random in this study. Formally, for angles quantized to intervals of 45° , the conditional probability density of the second-order combinations of two neighboring pixels separated by distance d can be derived from the following equations:

$$p(i, j, d, 0^\circ) = \#\{(x_1, y_1), (x_2, y_2) \in (L_r L_c)(L_r L_c) \text{ with } x_1 - x_2 = 0, |y_1 - y_2| = d, \text{ and } f(x_1, y_1) = i, f(x_2, y_2) = j\} \quad (2)$$

$$p(i, j, d, 45^\circ) = \#\{(x_1, y_1), (x_2, y_2) \in (L_r L_c)(L_r L_c) \text{ with } x_1 - x_2 = d, y_1 - y_2 = -d \text{ or } x_1 - x_2 = -d, y_1 - y_2 = d, \text{ and } f(x_1, y_1) = i, f(x_2, y_2) = j\} \quad (3)$$

$$p(i, j, d, 90^\circ) = \#\{(x_1, y_1), (x_2, y_2) \in (L_r L_c)(L_r L_c) \text{ with } |x_1 - x_2| = d, y_1 - y_2 = 0, \text{ and } f(x_1, y_1) = i, f(x_2, y_2) = j\} \quad (4)$$

$$p(i, j, d, 135^\circ) = \#\{(x_1, y_1), (x_2, y_2) \in (L_r L_c)(L_r L_c) \text{ with } x_1 - x_2 = d, y_1 - y_2 = -d \text{ or } x_1 - x_2 = -d, y_1 - y_2 = d, \text{ and } f(x_1, y_1) = i, f(x_2, y_2) = j\} \quad (5)$$

where # describes the element number in the set. In addition, i and j represent the gray values of pixels located at the (x_1, y_1) and (x_2, y_2) in the crack pattern, respectively. $p(i, j)$ refers to the element of the GLCM corresponding to the position of the i th row and the j th column, which reflects the probability of the simultaneous occurrence of gray level i and gray level j in the image. In order to describe the texture characteristics more scientifically, 12 specific texture features were calculated from the extracted GLCMs using the equations proposed by Haralick et al. [44], including contrast (CON), angular second moment (ASM), entropy (ENT), homogeneity (HOM), correlation (COR), cluster shade (CS), cluster prominence (CP), max probability (MP), sum average (SA), sum entropy (SE), sum variance (SV), and information of correlation (IC). Note that in order to effectively consider the computational complexity and fully maintain the GLCM texture information, five pixels were selected as the GLCM step size according to the research proposed by Zhao et al. [45]. Moreover, after considering the effect of the directions, the GLCM texture features computed from 0° , 45° , 90° , and 135° were averaged for further analysis.

In order to further simplify the expression of texture features on crack morphology with minimal loss of information, principal component analysis (PCA) was carried out in this study for the extracted GLCM texture features since PCA can replace older variables with fewer mutually independent new variables by using the idea of linear dimensionality reduction with less loss of information to preserve metadata features and data compression. Specifically, 12 CLCM texture features were firstly normalized in this study using SPSS 26.0, after that the normalized texture features were further subjected to principal component analysis.

2.6. Correlation Analysis and Regression Model Establishment

To quantitatively analyze the relationship between different soil parameters and crack characteristics, Pearson correlation coefficients were computed using the following equation between each soil salinity parameter and different types of crack characteristic parameters.

$$R = \frac{\sum_{i=1}^n (x_i - \bar{x}) \times (y_i - \bar{y})}{\sqrt{\sum_{i=1}^n (x_i - \bar{x}) \times \sum_{i=1}^n (y_i - \bar{y})}} \quad (6)$$

where x_i and y_i refer to the measured and fitted soil parameters of the soil samples and n stands for the number of soil samples. Note that y_i was calculated from linear regression models based on different types of characteristics.

In order to effectively estimate the soil salinity of salt-affected soils in the Songnen Plain, China, three prediction models including multiple linear regression (MLR), multiple stepwise regression (MSR), and artificial neural network (ANN) were developed based on different types of characteristics such as crack length, the box-counting dimension, and the first two principal components of GLCM texture features. Note that all 57 soil samples were rearranged in ascending order based on salinity levels. Afterwards, 38 soil samples were uniformly selected as the modeling dataset, and the remaining soil samples were used for validation. Specifically, both MLR and MSR were performed for the prediction of different soil parameters using the SPSS software (version 26.0), and the significant contribution levels of the variables $F \leq 0.05$ and $F \geq 0.10$ were set as the criteria for selecting and excluding variables from MSR, respectively. In addition, the most widely used BP neural network model was selected among all kinds of ANN methods, which covers a three-layer structured multilayer feed-forward back-propagation network including a topology consisting of an input layer, a single implicit layer, and an output layer [46–48]. For each output node corresponding to the soil parameter, the crack length, the box-counting fractal dimension, and the first two principal components of the texture features were selected as nodes for each input layer. Figure 6 shows a neuron model in a BP neural network, where x represents the input signal, w describes the connection weights, S refers to a linear combination of the weights and input signal, A is the tan-sigmoid transfer function of the neuron, and Y is the output signal. For different soil parameters, the maximum number of iterations of the training model was 1000, with an error threshold of 1.0×10^{-6} and a learning rate of 0.01. In addition, the number of implicit neurons varied systematically from two to six, and the most suitable network size for different soil salinity parameters was selected based on the performance of the test dataset [49].

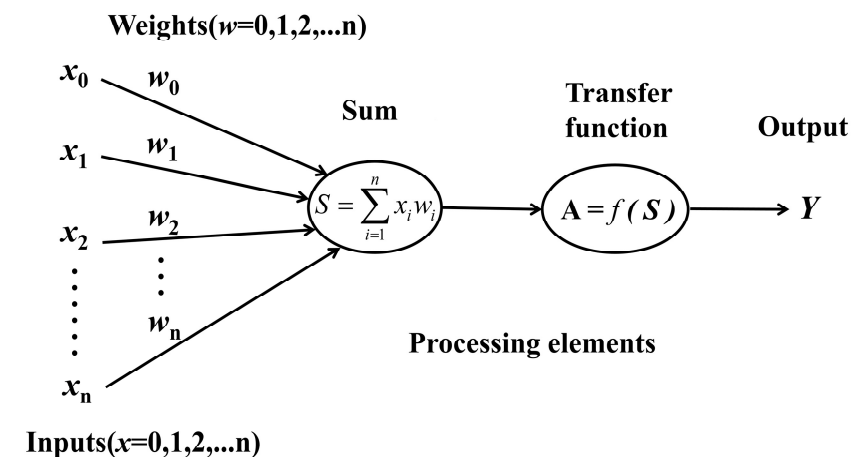


Figure 6. A simple schematic diagram of artificial neural network.

3. Results

3.1. Soil Physical and Chemical Properties

The statistical characteristics of the physical and chemical parameters of all the soil samples are shown in Table 1. Note that salinity refers to the sum of the ion content. From the table, it can be observed that Na^+ refers to the dominant cation, and CO_3^{2-} and HCO_3^- are the major anions, which covers the similar measurements obtained by Zhou et al. [50] and further confirms the results of mineralogy analysis in the Songnen Plain [51,52]. As seen from the table, the pH ranged from 8.01 to 10.77, the EC values of the samples ranged from 0.06 ds/m to 3.39 ds/m, and the ESP ranged from 0.26 to 47.30, indicating that most experimental samples in this study could be regarded as a typical type of Solonetz according to the international classification standard $\text{ESP} > 15\%$ and $\text{pH} > 8.5$ [53,54]. The soil salinity from 1.06 mg/g to 29.73 mg/g showed an extensive range in total salinity between soil samples, denoting significant differences in salinity. In addition, Table 1 also shows that the coefficients of variation of the physical and chemical parameters are apparent for different soil samples, reflecting the large degree of dispersion of all the soil samples. This therefore indicated that the selected samples were well representative and thus accurately described the distribution of soil properties in the study area.

Table 1. Statistical description of physical and chemical parameters of soil samples.

Soil Parameters	Min	Max	Mean	SD	CV (%)	Skewness	Kurtosis
pH	8.01	10.77	9.83	0.73	7.41	−1.14	0.18
EC (ds/m)	0.06	3.39	0.97	0.84	86.64	1.02	0.56
Na^+ (mg/g)	0.12	14.12	3.32	3.28	98.95	1.51	2.13
K^+ (mg/g)	0.01	0.06	0.02	0.01	67.41	2.14	5.49
Ca^{2+} and Mg^{2+} (mg/g)	0.10	1.60	0.53	0.32	59.75	1.19	1.67
HCO_3^- (mg/g)	0.12	5.00	1.57	0.99	63.40	1.11	1.38
CO_3^{2-} (mg/g)	0.00	5.50	1.75	1.56	89.33	1.02	0.14
Cl^- (mg/g)	0.08	5.25	1.32	1.46	110.44	1.34	0.86
Salinity (mg/g)	1.06	29.73	8.50	6.46	75.98	1.22	1.43
SAR	0.34	42.03	9.63	8.71	90.44	1.72	3.51
ESP (%)	0.26	47.30	10.58	9.91	93.67	1.67	3.43
Clay (%)	25.39	32.04	27.98	1.54	5.49	0.43	−0.27
Silt (%)	28.72	40.4	35.19	3.18	9.03	−0.12	−0.82
Sand (%)	28.26	43.94	36.85	3.64	9.87	−0.21	−0.85

N = 57; SD: standard deviation; CV: coefficient of variation.

3.2. Crack Characteristic Parameters

3.2.1. Crack Length

The statistical results of CL for 57 soil samples with desiccation cracks indicated that the crack lengths of all soil samples covered quite a large distribution from 200 cm to 797.18 cm with an average value of 444.26 cm. In addition, the standard deviation and coefficient of variation of all soil samples in this study were 120.65 cm and 27.16%, respectively, showing that the extent of desiccation cracking was quite random and fluctuating in a wide range, covering a similar range measured by Ren et al. [55].

3.2.2. Fractal Dimension

From the extraction results of the box-counting dimensions of all 57 soil samples, a minimum value of 1.27 and a maximum value of 1.69 were found in this study with a mean value of 1.55, representing quite a concentrated range. Moreover, the standard and the coefficient of variation were 0.09 and 5.63%, respectively, indicating relatively small fluctuations in the value of the fractal dimension, which is similar to the fractal dimension measurements measured by Zhang et al. [56] for the cracked soil surface in the Songnen Plain.

3.2.3. GLCM Texture Features

In Table 2, statistical parameters of 12 GLCM texture features in the binary images were listed for all 57 cracked soil samples. The table indicates that the distribution range of different types of texture features varied greatly and that all texture features were positive except for SV. Although the HOM and MP were low (4.252% and 11.421%, respectively), the CV of the other texture features was above 20%, denoting that the GLCM texture features of cracked soil samples were highly dispersed and well distinguished. In addition, the kurtosis and skewness coefficients for the different texture features ranged from -1.008 to 3.401 and -1.853 to 1.452 , respectively. From the extracted GLCM texture features and the GLCM texture analysis for desiccation cracking soils in natural conditions by Zhao et al. [45], it can be seen that although it differed slightly, the overall distribution of all 12 texture features was still poorly skewed and well-concentrated, which conformed to the characteristics of a normal distribution.

Table 2. Statistical results of 12 texture features of all cracked soil samples.

Texture Features	Min	Max	Mean	SD	CV (%)	Skewness	Kurtosis
CON	0.001	0.287	0.123	0.080	64.941	0.330	-1.006
ASM	0.430	0.999	0.761	0.151	19.820	-0.345	-0.842
ENT	0.009	1.552	0.712	0.398	55.830	0.185	-0.830
HOM	0.856	1.000	0.938	0.040	4.252	-0.332	-1.008
COR	0.007	0.297	0.089	0.065	72.981	1.452	1.894
CS	0.001	0.364	0.136	0.085	62.270	0.478	-0.042
SP	0.001	0.638	0.199	0.146	73.550	1.019	1.098
MP	0.612	0.999	0.860	0.098	11.421	-0.632	-0.432
SA	0.008	1.265	0.589	0.319	54.051	0.154	-0.757
SE	1.946	3.971	2.650	0.551	20.782	0.623	-0.571
SV	-0.156	-0.001	-0.029	-0.033	113.430	-1.853	3.401
IC	0.010	0.320	0.092	0.064	69.701	1.405	2.195

N = 57; SD: standard deviation; CV: coefficient of variation.

Figure 7 shows the cross-correlation coefficients among the 12 texture features from crack patterns of all 57 soil samples. As can be seen in the figure, different GLCM texture features were strongly correlated with high correlation coefficients, all above 0.85, indicating a large redundancy in the quantitative description of crack cracking status by the 12 textures, which thus increased the complexity of further analysis.

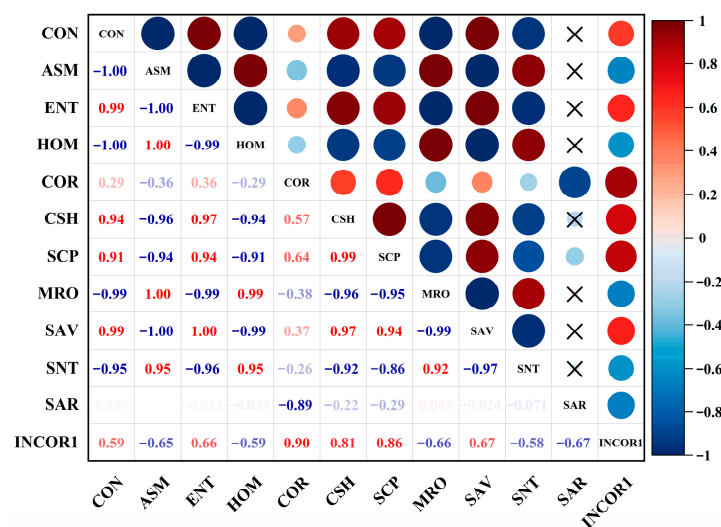


Figure 7. Correlation heatmap with GLCM texture features. Coefficients of correlation are presented on the side panel; positive correlations are labeled with red while negative correlations are labeled with blue color. Significant level: 0.05. Color intensity indicates strength of correlation. N = 57.

Table 3 indicates the PCA results of 12 GLCM texture features of all soil samples in this study. From the table, it can be seen that the first two principal components offered a cumulative contribution rate of 97.9% with eigenvalues of 9.45 and 2.30, respectively, showing that they can be considered effective components representing the GLCM texture features.

Table 3. Cumulative principal component eigenvalues and contribution rates of texture feature extraction.

Components	Initial Eigenvalue		
	Eigenvalue λ_i	Variance (%)	Cumulative Contribution Rate (%)
1	9.45	78.75	78.75
2	2.30	19.15	97.90
3	0.13	1.06	98.96
4	0.09	0.77	99.73
5	0.02	0.19	99.92
6	0.01	0.06	99.98
7	0.00	0.01	100.00
8	0.00	0.00	100.00
9	0.00	0.00	100.00
10	0.00	0.00	100.00
11	0.00	0.00	100.00
12	0.00	0.00	100.00

N = 57.

Table 4 presents the loading matrix of the GLCM texture features corresponding to the first two principal components, and the loading of each variable indicated its correlation with each principal component. The principal component coefficient was calculated as follows:

$$e_i = \frac{\alpha_i}{\sqrt{\lambda_i}} \quad (7)$$

where e_i represents the principal component coefficient, α_i describes the variable loading corresponding to each principal component, and λ_i refers to the eigenvalue corresponding to the principal component.

Table 4. The first two GLCM texture feature principal component loading matrices.

Variables	First Principal Component	Second Principal Component
CON	0.96	−0.23
ASM	−0.98	0.16
ENT	0.98	−0.16
HOM	−0.96	0.23
COR	0.50	0.85
CS	0.99	0.06
SP	0.97	0.15
MP	−0.98	0.13
SA	0.98	−0.15
SE	−0.93	0.24
SV	−0.16	−0.95
IC	0.77	0.60

N = 57.

The loading data and eigenvalues were then transformed into the following equations to calculate the principal component expressions further:

$$F_1 = 0.315Z_{CON} - 0.32Z_{ASM} + 0.321Z_{ENT} - 0.315Z_{HOM} + 0.165Z_{COR} + 0.323Z_{CSH} + 0.318Z_{SCP} - 0.319Z_{MRO} + 0.321Z_{SAV} - 0.304Z_{SNT} - 0.055Z_{SAR} + 0.25Z_{INCOR1} \quad (8)$$

$$F_2 = -0.153Z_{CON} + 0.108Z_{ASM} - 0.109Z_{ENT} + 0.153Z_{HOM} + 0.563Z_{COR} + 0.046Z_{CSH} + 0.102Z_{SCP} + 0.088Z_{MRO} - 0.099Z_{SAV} + 0.16Z_{SNT} - 0.631Z_{SAR} + 0.397Z_{INCOR1} \quad (9)$$

where F_1 and F_2 represent the first and second principal components of the GLCM texture features, and Z refers to the normalized GLCM texture features. The principal component values of the texture features of the 57 samples were calculated based on principal component expressions.

3.3. Correlation Analysis

Table 5 shows the correlation coefficients of different soil salinity parameters with the CL, the box-counting dimension, and the first two principal components of the GLCM texture features. The table shows that the soil parameters were all positively correlated with the cracking parameters. In addition, Table 5 also shows the highest correlation coefficient of 0.88 between the CL and the total salt content.

Table 5. Correlation coefficient matrix of soil salinity parameters and crack characteristics.

Soil Salinity Parameters	CL	D	F ₁	F ₂
pH	0.64	0.50	0.59	−0.26
EC (ds/m)	0.87	0.57	0.59	−0.62
Na ⁺ (mg/g)	0.87	0.51	0.52	−0.40
K ⁺ (mg/g)	0.24	0.29	0.29	−0.05
Ca ²⁺ and Mg ²⁺ (mg/g)	0.24	0.10	0.26	−0.02
HCO ₃ [−] (mg/g)	0.60	0.51	0.65	−0.08
CO ₃ ^{2−} (mg/g)	0.73	0.37	0.25	−0.62
Cl [−] (mg/g)	0.82	0.48	0.46	−0.41
Salinity (mg/g)	0.88	0.54	0.53	−0.45
Clay (%)	0.14	0.30	0.20	−0.05

N = 57; CL: crack length; D: box-counting dimension; F₁: the first principal component of GLCM texture features; F₂: the second principal component of GLCM texture features.

It can also be seen from Table 5 that the box-counting fractal dimension was the most strongly correlated with EC among all soil salinity parameters, with a correlation coefficient of 0.57. In addition, the first principal component of the texture features also showed a high correlation with most soil parameters, whereas the highest correlation coefficients were found between the second principal of GLCM texture features and CO₃^{2−}, EC, which were significantly higher than those with salinity, Cl[−], Na⁺, and pH. Moreover, the correlation coefficients with K⁺, Ca²⁺, and Mg²⁺ were very low, from 0.02 to 0.29, with all kinds of crack characteristics, indicating that the crack characteristics did not show a good response to these salinity parameters of salt-affected soils in this study.

3.4. Soil Salinity Parameter Prediction Models

3.4.1. Multiple Linear Regression Model

Table 6 represents the MLR models for different soil salinity parameters. As can be seen from the table, Na⁺, EC, and total salt content were modeled with high accuracy with R² values of 0.83, 0.86, and 0.89, respectively, followed by the major anions CO₃^{2−} and Cl[−], with an R² of 0.72 and 0.79, respectively. Although multiple linear regression methods could also predict HCO₃[−] and pH, the R² of 0.46 and 0.48 indicated limited prediction accuracy. Moreover, Table 6 also indicates that the worst prediction accuracy was found for K⁺, Ca²⁺, and Mg²⁺ with an R² of only 0.07 and 0.18, respectively.

3.4.2. Multiple Stepwise Regression Model

Table 7 lists the variables of the best model retained for the different soil parameters when multiple stepwise regressions were performed. As seen in Table 7, the CL was the only influencing factor for pH, HCO₃[−], Cl[−], and salinity. For EC, two independent variables of CL and the second principal component of the texture features were selected as variables, and Na⁺ and CO₃^{2−} were multivariate linearly modeled by excluding only one crack characteristic. However, because of their limited contents, all types of crack

parameters did not show sufficient contribution and thus were not selected as effective variables for the prediction models of K^+ , Ca^{2+} , and Mg^{2+} .

Table 6. Multiple linear regression of soil parameters and cracking parameters.

Soil Parameters	Formulas	R	R ²
pH	$Y = 13.272 + 0.003 X_1 - 2.992 X_2 + 0.126 X_3 - 0.038 X_4$	0.69	0.48
EC	$Y = -3.443 + 0.008 X_1 + 0.570 X_2 - 0.054 X_3 + 0.123 X_4$	0.93	0.86
Na ⁺	$Y = -13.421 + 0.034 X_1 + 1.202 X_2 - 0.299 X_3 + 0.623 X_4$	0.91	0.83
K ⁺	$Y = 0.034 - 5.634 \times 10^{-6} X_1 - 0.01 X_2 - 0.001 X_3$	0.26	0.07
Ca ²⁺ and Mg ²⁺	$Y = 3.465 - 1.953 X_2 + 0.079 X_3 + 0.10 X_4$	0.42	0.18
HCO ₃ ⁻	$Y = 5.98 + 0.003 X_1 - 3.807 X_2 + 0.191 X_3 + 0.079 X_4$	0.68	0.46
CO ₃ ²⁻	$Y = -15.078 + 0.012 X_1 + 7.361 X_2 - 0.395 X_3 - 0.004 X_4$	0.85	0.72
Cl ⁻	$Y = -9.221 + 0.014 X_1 + 2.903 X_2 - 0.157 X_3 - 0.182 X_4$	0.89	0.79
Salinity	$Y = -28.225 + 0.063 X_1 + 5.689 X_2 - 0.579 X_3 + 0.89 X_4$	0.94	0.89

N = 38; X₁: crack length; X₂: box-counting dimension; X₃: the first principal component of GLCM texture features; X₄: the second principal component of GLCM texture features.

Table 7. Variables retained in multiple stepwise regression for each soil parameter.

Soil Parameters	CL	D	F ₁	F ₂
pH	✓	×	×	×
EC	✓	×	×	✓
Na ⁺	✓	×	✓	✓
K ⁺	-	-	-	-
Ca ²⁺ and Mg ²⁺	-	-	-	-
HCO ₃ ⁻	✓	×	×	×
CO ₃ ²⁻	✓	✓	✓	×
Cl ⁻	✓	×	×	×
Salinity	✓	×	×	×

N = 38; CL: crack length; D: box-counting dimension; F₁: the first principal component of GLCM texture features; F₂: the second principal component of GLCM texture features.

The prediction models and accuracy of different soil salinity parameters derived from multiple stepwise regression analyses were listed in Table 8, showing that the model accuracy remained the highest for the total salinity with an R² of 0.86 and that Na⁺ and EC were also well predicted with R² values of 0.83 and 0.85, respectively. In addition, R² values of 0.76 and 0.72 described the accuracy of Cl⁻ and CO₃²⁻ prediction. However, the multiple stepwise regression method was not used to estimate the pH and HCO₃⁻ because of the poor prediction R² of only 0.42 and 0.36.

Table 8. Multiple stepwise regression model and accuracy.

Soil Parameters	Formulas	R	R ²
pH	$Y = 8.197 + 0.004 X_1$	0.65	0.42
EC	$Y = -2.12 + 0.007 X_1 + 0.08 X_4$	0.92	0.85
Na ⁺	$Y = -11.535 + 0.034 X_1 + 0.613 X_3 - 0.267 X_4$	0.91	0.83
K ⁺	-	-	-
Ca ²⁺ and Mg ²⁺	-	-	-
HCO ₃ ⁻	$Y = 1.475 + 0.169 X_3$	0.60	0.36
CO ₃ ²⁻	$Y = -15.128 + 0.012 X_1 - 0.396 X_3 + 7.378 X_2$	0.85	0.72
Cl ⁻	$Y = -3.47 + 0.011 X_1$	0.87	0.76
Salinity	$Y = -12.908 + 0.049 X_1$	0.93	0.86

N = 38; X₁: crack length; X₂: box-counting dimension; X₃: the first principal component of texture features; X₄: the second principal component of texture features.

3.4.3. BP Neural Network Model

The specific number of iterations, number of neurons, and the R^2 of the modeling results selected for the BP neural network model are listed in Table 9. It can be seen that the model accuracy for both Na^+ and salinity was greater than 0.9. Table 9 also indicates that good accuracy also can be found for predicting Cl^- and EC since the corresponding R^2 was 0.85 and 0.87, respectively. In addition, the modeling results of R^2 values of 0.75 and 0.62 for CO_3^{2-} and pH indicated that only a relatively coarse estimation was made using BP neural networks. Moreover, it can also be seen from Table 9 that the predictive abilities of HCO_3^- , K^+ , Ca^{2+} , and Mg^{2+} were poor, with R^2 values of only 0.47, 0.27, and 0.24, respectively.

Table 9. BP neural network modeling accuracy and network parameters.

Soil Parameters	Number of Iterations	Number of Neurons	R	R^2
pH	13	4	0.79	0.62
EC	11	4	0.93	0.87
Na^+	10	4	0.96	0.92
K^+	14	3	0.52	0.27
Ca^{2+} and Mg^{2+}	12	3	0.49	0.24
HCO_3^-	10	4	0.69	0.47
CO_3^{2-}	13	2	0.87	0.75
Cl^-	9	3	0.92	0.85
Salinity	13	4	0.97	0.94

N = 38.

4. Discussion

4.1. Effects of Salinity on the Desiccation Cracking Process

Many research studies have revealed that mechanical properties such as suction, surface energy, and tensile strength can largely determine the desiccation cracking process of clayey saline soils, which are mainly affected by physical–chemical properties of salt-affected soils including the clay mineral types, the clay contents, and the salinity levels [57–60]. However, both mineral type and clay content were not found to determine the desiccation cracking process of salt-affected soil in the Songnen Plain, China. This is because the clay content has a low impact on the soil cracking process due to the small concentration of soil samples ranging from 25.39% to 32.04% with a standard deviation of only 1.54%, and the results are very close to those found by Wang et al. [61] and Zhang et al. [62]. Moreover, the measurements from Zhang et al. also revealed that the main primary minerals of salt-affected soils in the Songnen Plain, China, are feldspar and quartz, and that illite/smectite formation with an inter-layer ratio above 0.5 is found as the main type of secondary mineral; in addition, clay minerals of this type are very inactive, with an activity index of only 0.33 to 0.48, denoting that both the content and mineral composition of the clay have almost no impact on the desiccation cracking process of salt-affected soils in this region. Specifically, the relationship between the clay content and the different crack characteristics was further analyzed in this study, as shown in Figure 8. The scatter diagrams in Figure 8 show that no regularity can be found for the data distribution, showing that clay content is not sensitive to the desiccation cracks generated on the surface of salt-affected soils in the Songnen Plain, which also concurs with the research of Wang et al. [61] and Zhang et al. [62].

As shown in Table 1, the high SAR and ESP of the soil samples show that Na^+ is the dominant cation compared with K^+ , Ca^{2+} , and Mg^{2+} . In addition, the correlation coefficients listed in Table 5 also indicate that the soil salinity parameters are significantly and positively correlated with different soil surface crack characteristics, showing that soil salinity is the dominant factor in determining the shrinkage and cracking conditions. In particular, the exchangeable cations (especially for the Na^+ with a large hydrolytic radius) interact with soil particles during the dehydration process of the saturated slurry of salt-affected soil samples in this study area. After that, a prominent bound water film is then

formed between various soil particles and largely increases the distance between them. This kind of water-bounding film can be thickened due to the content of exchangeable cations, which thus reduces the shear and tensile strength between different colloidal soil particles, and also decreases the cementation of the salt-affected soils [63]. At the same time, the internal friction angle is also reduced between different soil particles due to the effect of the salt solution lubricant raised by soil salinity, indicating that the extent of shear resistance was further weakened in the soil samples. In addition, after analyzing the effect of soil salt content on the surface shrinkage–cracking process from the perspective of the diffusion double layer (DDL), DeCarlo et al. [32] and Shokri et al. [64] showed that the increasing soil salinity could significantly reduce the thickness of DDL, which in turn reduces the strength of the soil and further promotes the shrinkage and cracking of cohesive salt-affected soils in the Songnen Plain, China.

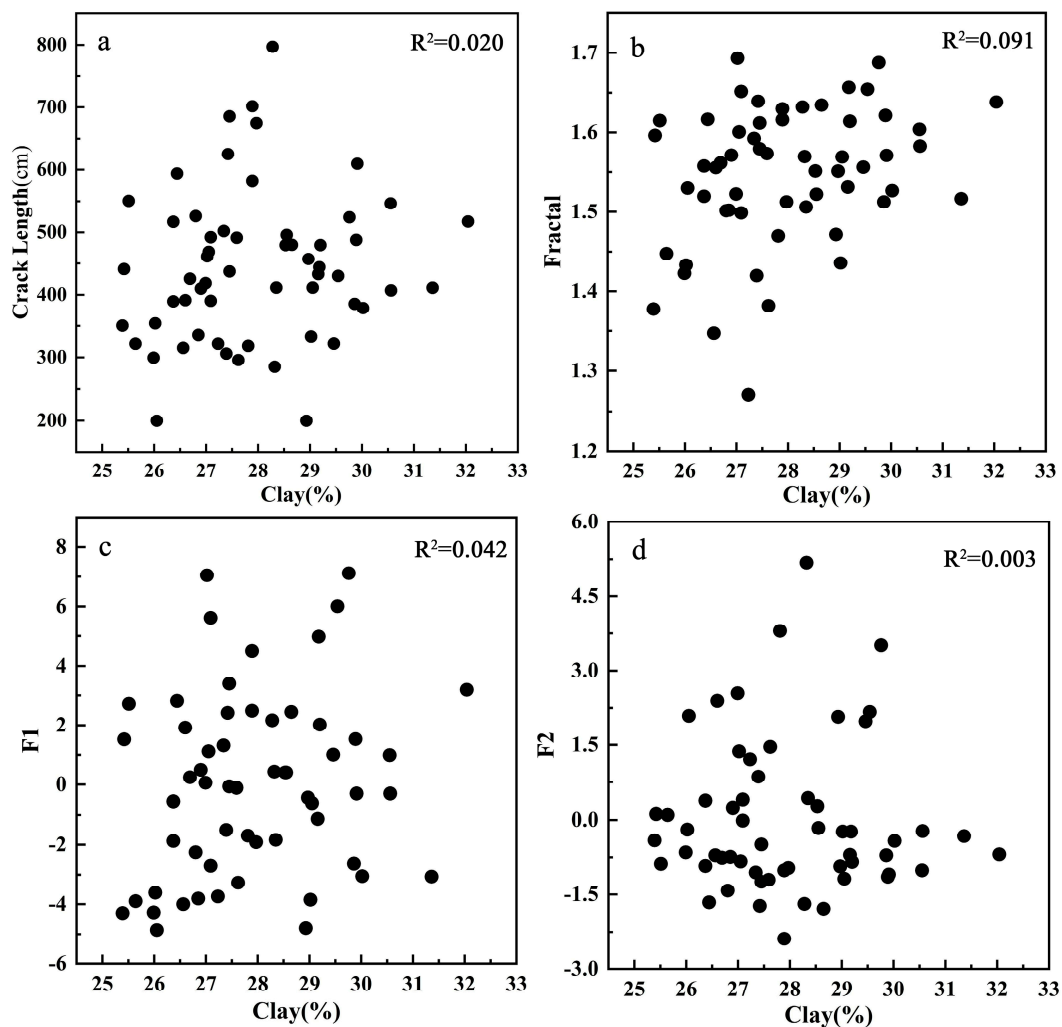


Figure 8. Scatter diagrams between clay content and different crack characteristics. (a) Crack length, (b) box-counting dimension, (c) first component of GLCM texture features, (d) second component of GLCM texture features.

4.2. Prediction Abilities of Different Models

As a single type of crack parameter is often unable to describe the process of desiccation cracking fully, three different kinds of common crack characteristics were selected to comprehensively quantify the cracking condition of the soil surface in this study. Among them, CL is the most commonly used characterization index of crack characteristics, which can visually determine the extent of desiccation cracks generated on the soil surface. The

fractal dimension can quantitatively describe the autocorrelation and complexity of the crack morphology, and texture features can effectively describe the spatial distribution and the structural arrangement information of soil desiccation cracks. The correlation coefficients (R values) between the measured and estimated soil properties shown in Tables 6, 8, and 9 were notably higher than those shown in Table 5 since the results in Table 5 also represented the relationship between the measured soil properties and the predicted soil properties based on the linear model. Therefore, modeling approaches integrating different types of crack characteristics are more relevant and applicable than prediction results based on only one particular crack parameter.

It can be seen from the regression models developed in Tables 6, 8, and 9 that the three models combining different types of crack characteristics have better modeling accuracy for the total salt content, EC, and Na^+ (R^2 values are all greater than 0.83) compared with other soil properties in this study. Although specific prediction abilities can be guaranteed, the prediction accuracy of Cl^- , HCO_3^- , CO_3^{2-} , and pH is quite different for different models, and the overall prediction accuracy shows a tendency of $\text{Cl}^- > \text{CO}_3^{2-} > \text{pH} > \text{HCO}_3^-$ because CO_3^{2-} and HCO_3^- are easily hydrolyzed in solution with a reversible process, indicating that the contents of these two ions are very unstable. In addition, none of the models showed good prediction accuracy for K^+ , Ca^{2+} , or Mg^{2+} , with R^2 values below 0.28. This is because the very low contents of these cations in the Songnen Plain had a lower impact on the soil cracking process than Na^+ , thus showing a poor correlation with the soil cracking characteristics.

Multiple stepwise regression analysis was performed using multiple linear regressions. Specifically, after comparing the contribution rate of the independent variables to the dependent variable, the variables with a large contribution rate were selected via the MSR method according to their importance in this study. Table 8 indicates that the multiple stepwise regression method leads to some crack characteristics being ignored owing to their low contribution, resulting in the overall prediction accuracy of the soil salinity parameters being lower than those of the other two models. For parameters with low contents of K^+ , Ca^{2+} , and Mg^{2+} , modeling may not be achieved because all crack characteristic variables cannot reach the selection criteria. In general, multiple stepwise regression analysis can achieve optimization of multiple linear regression methods in many cases and achieve model simplification and variable compression in the case of a large number of independent variables. However, this study included only four independent variables in the model. In addition, the crack characteristics were rarely correlated, showing that using multiple stepwise regression may ignore the role of certain crack features, resulting in the low prediction accuracy of soil parameters.

As a traditional method, multiple linear regression can offer fast prediction speed with a simple structure, which is commonly used to analyze the influence of different crack parameters. In addition, this type of method can remove autocorrelation and multicollinearity between other variables with accurate prediction results. However, this method usually does not express the complex nonlinear relationships between different variables well and also requires the treatment of the characteristic variables when the variables are very smooth or correlated with each other.

As shown in Tables 6 and 9, BP neural networks significantly improve the prediction accuracy of all soil parameters compared to multiple linear regression. This is because the BP neural network has a strong memory ability and can find optimal solutions through autonomous learning. However, the artificial neural network method also relies on large amounts of data, indicating that the prediction results can be inaccurate when the data are insufficient. In addition, the method also needs to manually adjust the network parameters and nodes, denoting that improper operations can reduce the accuracy of the prediction results.

In order to further compare the prediction accuracy of different models for estimating salinity parameters of soda-salt-affected soils in the Songnen Plain, China, validation work was also carried out in this study using 19 soil samples. Table 10 shows the accuracy of the

three prediction models for different salinity parameters of all 19 validation soil samples, where R^2 indicates the fit degree between the measured and estimated soil parameters related to salinity, and the ratio of performance to deviation (RPD) is used to analyze the degree of match between the measured and estimated values. Table 10 also indicates that for most soil parameters in this study, BP neural networks can be found with a higher overall prediction accuracy compared with the multiple linear method and the multiple stepwise method. Specifically, from the criteria proposed by Farifteh et al. [65], it can be seen that the BP neural network method is accurate in predicting EC and Na^+ because the R^2 and RPD are above 0.91 and 2.5, respectively; the validation results of soil salinity also satisfy the criteria of R^2 above 0.81 and RPD above 2.5, showing that the BP neural network method also has a relatively good prediction ability. In addition, a specific prediction ability can be reached for Cl^- , CO_3^{2-} , HCO_3^- , and pH since R^2 for all of these soil parameters was found to be above 0.6, but the low RPD values indicated that the predicted results were not stable. Table 10 also shows that although the prediction accuracy of these soil parameters can be largely improved by the ANN method rather than the MLR method and the MSR method, the R^2 and RPD of the estimation results are still very low for K^+ , Ca^{2+} , and Mg^{2+} and thus cannot achieve adequate accuracy.

Table 10. Indicators of prediction accuracy of soil salinity parameters under different modeling methods.

Method	Index	pH	EC	Na^+	K^+	Ca^{2+} and Mg^{2+}	HCO_3^-	CO_3^{2-}	Cl^-	Salinity
MLR	R^2	0.55	0.85	0.90	0.14	0.02	0.72	0.67	0.58	0.91
	RPD	0.85	2.47	3.11	0.45	0.44	0.69	1.49	1.36	3.15
MSR	R^2	0.49	0.89	0.87	-	-	0.53	0.66	0.63	0.92
	RPD	1.32	3.06	2.21	-	-	1.33	1.69	1.44	3.38
ANN	R^2	0.66	0.91	0.91	0.22	0.28	0.65	0.71	0.62	0.89
	RPD	1.06	2.96	3.47	0.40	0.60	0.84	1.50	1.58	2.95

N = 19; MLR: multiple linear regression; MSR: multiple stepwise regression; ANN: artificial neural networks.

To further evaluate the predictive ability of the BP neural network method for the soil parameters of salt-affected soils in this study, the predicted results computed from the BP neural network method were linearly fitted to the measured results based on a $y = x$ function (Figure 9).

According to the fitting results in Figure 9 and the range of soil parameters in Table 1, the soil samples are well represented. The fitting function of the model is very close to the actual relationship between the soil parameters and the crack characteristics. In addition, Figure 9 indicates that the BP neural network method can combine different types of crack characteristics, which can be used to measure saline soil parameters quickly and effectively such as Na^+ , EC, and salt content with high prediction accuracy. Note that the generalization ability of the BP neural network is largely affected by the number and the representativeness of the soil samples. If there are more representative training samples, the fitting function of the model will be closer to the actual relationship between the soil parameters and the crack characteristics. Therefore, in future research, both the types of crack characteristics and the number of network training samples can be increased, and the most appropriate network types with different soil saline parameters can also be selected based on the performance of the test dataset to improve the application potential and accuracy of this method in the online field measurement of cracked soil saline parameters. Moreover, the most suitable neural network types with different soil salinity parameters can be selected according to the performance of the test dataset, which can further improve the accuracy and application potential of the proposed method in the online field measurement of salinity parameters for salt-affected soils. Despite the high accuracy of the above prediction models, it is still necessary to improve the models under natural conditions in future research. Specifically, the prediction of salt information throughout the entire region should be further achieved and verified within a large region through the interpolation method. In addition, the influencing factors of crack production (such as climate, topography, hydrology, and drying–

wetting cycles) should also be considered in future research to improve the prediction model with the aim of ultimately achieving the synchronous and large-scale accurate measurement of soil salt salinity parameters through combining different remote sensing scales based on point spread function, resampling method, and error transfer theory.

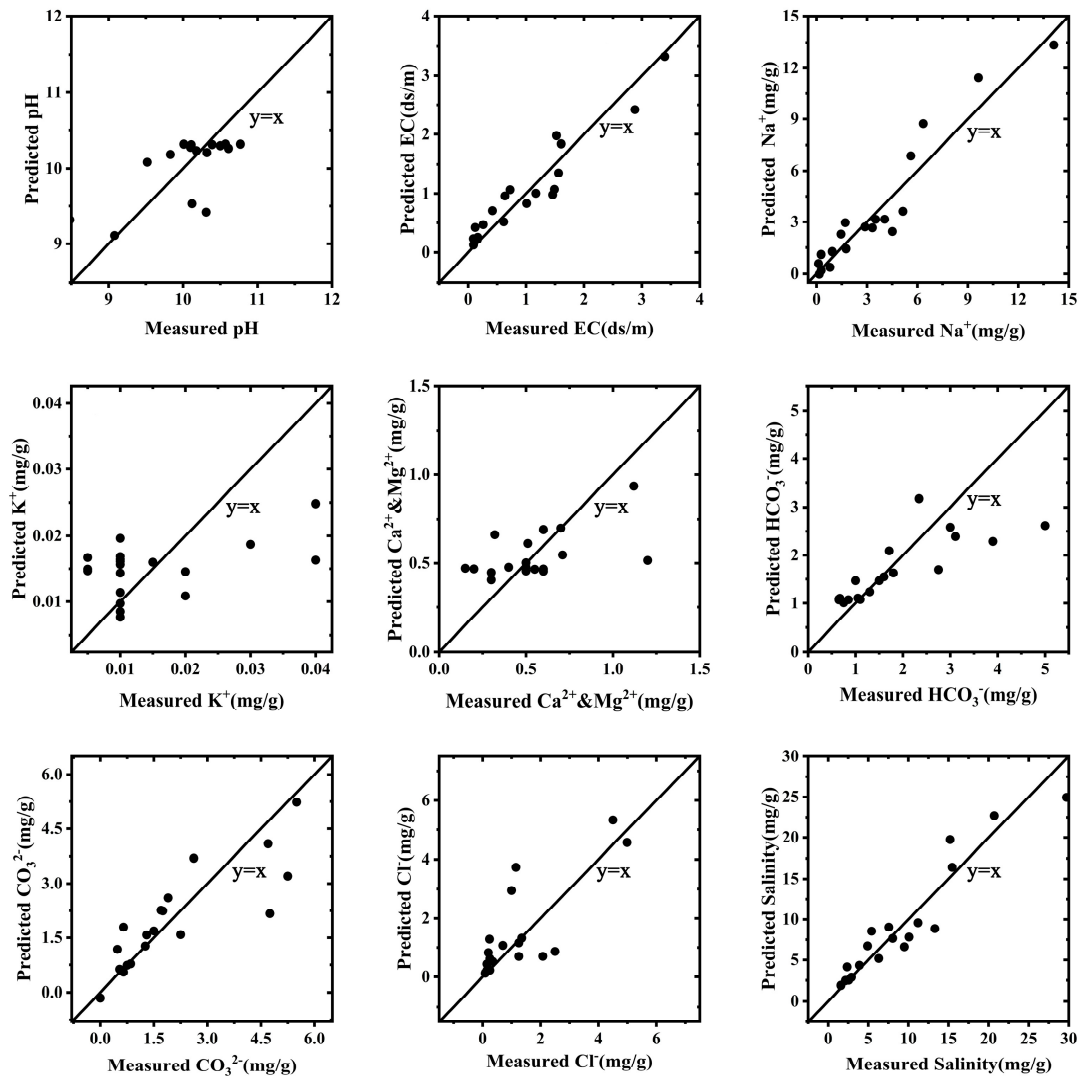


Figure 9. Fitting results of measured and predicted values using BP neural network method.

5. Conclusions

In this study, a laboratory soil cracking experiment was designed to quantitatively simulate the shrinkage–cracking process of salt-affected soils in the Songnen Plain, China. The results provided basic information for understanding the mechanism of the desiccation cracking process of saline-sodic soil and the relationship between soil salinity and different types of crack characteristics. In conclusion, Na⁺ was considered as the dominant role affecting the cracking process. The water film generated due to exchangeable cations reduced the tensile strength, the friction angle, and the cementation between soil particles, which promoted the desiccation cracking. The increasing thickness of DDL caused by soil salinity also made the surface of cohesive saline-sodic soil more prone to cracking. Regression models combining different types of crack characteristics can effectively predict the salinity parameters of salt-affected soils. Artificial neural networks can estimate the salinity parameters of salt-affected soils with a certain accuracy compared with multiple linear regression and multiple stepwise regression, particularly for predicting Na⁺, EC, and total soil salinity (R^2 from 0.89 to 0.91, RPD from 2.95 to 3.47), thereby showing great

importance for improving the salt-affected soils, ensuring food security, and enhancing the local environment. Future work includes investigating the deep mechanism of soil salinity on the desiccation cracking process based on the consideration of other factors such as climate, topography, and hydrological characteristics, and achieving the synchronous measurement of soil salt information at different scales.

Author Contributions: Conceptualization, X.L. and J.R.; methodology, J.R.; software, Z.Z.; validation, Z.Z. and Y.Z.; formal analysis, S.Z. and Y.Z.; investigation, J.R.; resources, X.L.; data curation, Z.Z.; writing—original draft preparation, Z.Z.; writing—review and editing, J.R. and S.Z.; visualization, Z.Z.; supervision, X.L.; project administration, J.R.; funding acquisition, J.R. and X.L. All authors have read and agreed to the published version of the manuscript.

Funding: This research was supported by the Fundamental Research Funds for the Central Universities of China (No. 2022-KYYWF-0156), the Graduate Innovative Research Project of Harbin Normal University (No. HSDSSCX2022-05), the Strategic Priority Research Program of the Chinese Academy of Sciences (No. XDA28110501), and the University Nursing Program for Young Scholars with Creative Talents in Heilongjiang Province of China (No. UNPYSCT-2018180).

Data Availability Statement: Not applicable.

Acknowledgments: We authors all appreciate the assistance provided by Zhichun Wang from the Da'an Alkaline Ecological Experimental Station, Chinese Academy of Sciences for the measurements of soil properties.

Conflicts of Interest: The authors declare no conflict of interest.

References

- Dai, Y.; Guan, Y.; Zhang, Q.; Sun, J.; He, X. Remote sensing monitoring and temporal and spatial characteristics of soil salinization in Aral Reclamation area. *Arid Land. Geogr.* **2022**, *45*, 1176–1185. (In Chinese)
- Boudibi, S.; Sakaa, B.; Benguega, Z.; Fadlaoui, H.; Othman, T.; Bouzidi, N. Spatial prediction and modeling of soil salinity using simple cokriging, artificial neural networks, and support vector machines in El Outaya plain, Biskra, southeastern Algeria. *Acta Geochim.* **2021**, *40*, 390–408. [\[CrossRef\]](#)
- Seo, B.; Jeong, Y.; Baek, N.; Park, H.; Yang, H.; Park, S.; Choi, W. Soil texture affects the conversion factor of electrical conductivity from 1:5 soil-water to saturated paste extracts. *Pedosphere* **2022**, *32*, 905–915. [\[CrossRef\]](#)
- Ding, J.; Yu, D. Monitoring and evaluating spatial variability of soil salinity in dry and wet seasons in the Werigan–Kuqa Oasis, China, using remote sensing and electromagnetic induction instruments. *Geoderma* **2014**, *235*, 316–322. [\[CrossRef\]](#)
- Khadim, F.K.; Su, H.; Xu, L.; Tian, J. Soil salinity mapping in Everglades National Park using remote sensing techniques and vegetation salt tolerance. *Phys. Chem. Earth* **2019**, *110*, 31–50. [\[CrossRef\]](#)
- Wang, F.; Yang, S.; Wei, Y.; Shi, Q.; Ding, J. Characterizing soil salinity at multiple depth using electromagnetic induction and remote sensing data with random forest: A case study in Tarim River Basin of southern Xinjiang, China. *Sci. Total Environ.* **2021**, *754*, 142030. [\[CrossRef\]](#)
- Yang, F.; An, F.; Ma, H.; Yang, H.; Wang, Z. Spatial variations of apparent soil electrical conductivity in the saline-sodic upland soil of the Songnen Plain. *Acta Ecol. Sin.* **2017**, *37*, 1184–1190. (In Chinese)
- Zarai, B.; Walter, C.; Michot, D.; Montoroi, J.P.; Hachicha, M. Integrating multiple electromagnetic data to map spatiotemporal variability of soil salinity in Kairouan region, Central Tunisia. *J. Arid Land* **2022**, *14*, 186–202. [\[CrossRef\]](#)
- Heil, K.; Schmidhalter, U. Comparison of the EM38 and EM38-MK2 electromagnetic induction-based sensors for spatial soil analysis at field scale. *Comput. Electron. Agric.* **2015**, *110*, 267–280. [\[CrossRef\]](#)
- Herrero, J.; Hudnall, W.H. Measurement of soil salinity using electromagnetic induction in a paddy with a densic pan and shallow water table. *Paddy Water Environ.* **2014**, *12*, 263–274. [\[CrossRef\]](#)
- Khongnawang, T.; Zare, E.; Srihabun, P.; Triantafilis, J. Comparing electromagnetic induction instruments to map soil salinity in two-dimensional cross-sections along the Kham-reen Canal using EM inversion software. *Geoderma* **2020**, *377*, 114611. [\[CrossRef\]](#)
- Alexakis, D.D.; Daliakopoulos, I.N.; Panagea, I.S.; Tsanis, I.K. Assessing soil salinity using WorldView-2 multispectral images in Timpaki, Crete, Greece. *Geocarto Int.* **2016**, *33*, 321–338. [\[CrossRef\]](#)
- Wang, Z.; Zhang, F.; Zhang, X.; Chan, N.; Wang, Y. Regional suitability prediction of soil salinization based on remote-sensing derivatives and optimal spectral index. *Sci. Total Environ.* **2021**, *775*, 145807. [\[CrossRef\]](#)
- Ghazali, M.F.; Wikantika, K.; Harto, A.B. Potential use of spectral analysis to delineate coastal boundary of a landmass based on estimation soil salinity and salt water intrusion: A preliminary result. *J. Coast. Conserv.* **2022**, *26*, 25. [\[CrossRef\]](#)
- Shahrayini, E.; Noroozi, A.A.; Eghbal, M.K. Prediction on soil properties by visible and near-infrared reflectance spectroscopy. *Eurasian Soil Sci.* **2020**, *53*, 1760–1772. [\[CrossRef\]](#)

16. Xu, L.; Wang, Z.; Hu, J.; Wang, S.; Nyongesah, J.M. Estimation of soil salinity under various soil moisture conditions using laboratory based thermal infrared spectra. *J. Indian Soc. Remote* **2021**, *49*, 959–969. [[CrossRef](#)]
17. Zovko, M.; Romić, D.; Colombo, C.; Iorio, E.D.; Romić, M.; Buttafuoco, G.; Castrignano, A. A geostatistical Vis-NIR spectroscopy index to assess the incipient soil salinization in the Neretva River valley, Croatia. *Geoderma* **2018**, *332*, 60–72. [[CrossRef](#)]
18. Fan, X.; Liu, Y.; Tao, J.; Weng, Y. Soil salinity retrieval from advanced multi-spectral sensor with partial least square regression. *Remote Sens.* **2015**, *7*, 488–511. [[CrossRef](#)]
19. Manickam, L.; Subramanian, D.; Khandal, S.; Hegde, R. Modeling and mapping of salt-affected soils through spectral indices in inland plains of semi-arid agro-ecological region. *J. Indian Soc. Remote* **2021**, *49*, 1475–1481. [[CrossRef](#)]
20. Nguyen, K.; Liou, Y.; Tran, H.; Hoang, P.; Nguyen, T. Soil salinity assessment by using near-infrared channel and vegetation soil salinity index derived from landsat 8 OLI data: A case study in the Tra Vinh Province, Mekong Delta, Vietnam. *Prog. Earth Planet. Sc.* **2020**, *7*, 1. [[CrossRef](#)]
21. Allbed, A.; Kumar, L.; Sinha, P. Soil salinity and vegetation cover change detection from multi-temporal remotely sensed imagery in Al Hassa Oasis in Saudi Arabia. *Geocarto Int.* **2018**, *33*, 830–846. [[CrossRef](#)]
22. Gorji, T.; Sertel, E.; Tanik, A. Monitoring soil salinity via remote sensing technology under data scarce conditions: A case study from Turkey. *Ecol. Indic.* **2017**, *74*, 384–391. [[CrossRef](#)]
23. Ma, L.; Ma, F.; Li, J.; Gu, Q.; Yang, S.; Wu, D.; Feng, J.; Ding, J. Characterizing and modeling regional-scale variations in soil salinity in the arid oasis of Tarim Basin, China. *Geoderma* **2016**, *305*, 1–11. [[CrossRef](#)]
24. El-Battay, A.; Bannari, A.; Hameid, N.A.; Abahussain, A.A. Comparative study among different semi-empirical models for soil salinity prediction in an arid environment using OLI Landsat-8 data. *Adv. Remote Sens.* **2017**, *6*, 23–39. [[CrossRef](#)]
25. Li, H.; Webster, R.; Shi, Z. Mapping soil salinity in the Yangtze delta: REML and universal kriging (E-BLUP) revisited. *Geoderma* **2015**, *237*, 71–77. [[CrossRef](#)]
26. Wu, W.; Al-Shafie, W.; Mhaimed, A.; Ziadat, F.; Nangia, V.; Payne, W. Soil salinity mapping by multiscale remote sensing in Mesopotamia, Iraq. *IEEE J. Sel. Top. Appl. Earth Obs. Remote Sens.* **2014**, *7*, 4442–4452. [[CrossRef](#)]
27. Yang, B.; Liu, J.; Zhao, X.; Zheng, S. Evaporation and cracked soda soil improved by fly ash from recycled materials. *Land Degrad. Dev.* **2021**, *32*, 2823–2832. [[CrossRef](#)]
28. Tang, C.; Zhu, C.; Cheng, Q.; Zeng, H.; Xu, J.; Tian, B.; Shi, B. Desiccation cracking of soils: A review of investigation approaches, underlying mechanisms, and influencing factors. *Earth-Sci. Rev.* **2021**, *216*, 103586. [[CrossRef](#)]
29. Lima, L.A.; Grismer, M.E. Soil crack morphology and soil salinity. *Soil Sci.* **1992**, *153*, 149–153. [[CrossRef](#)]
30. Sun, K.; Tang, C.; Wang, P.; Wang, D.; Chen, Z.; Xu, S. Effect of salt content on desiccation cracking behavior of soil. *J. Eng. Geol.* **2015**, *23*, 77–83. (In Chinese)
31. Chang, K.; Xing, X. Water characteristic curve and shrinkage characteristics of different sodification degree. *Chin. J. Irrig Drain.* **2021**, *40*, 131–136. (In Chinese)
32. Decarlo, K.F.; Shokri, N. Salinity effects on cracking morphology and dynamics in 3-D desiccating clays. *Water Resour. Res.* **2014**, *50*, 3052–3072. [[CrossRef](#)]
33. Xing, X.; Ma, X.; Kang, D. Impacts of type and concentration of salt cations on soil water retention and desiccation cracking. *Trans. Chin. Soc. Agric. Eng.* **2016**, *32*, 115–122. (In Chinese)
34. Huang, Y.; Zhang, Y.; Yang, M.; Zheng, Q.; Lin, J.; Jiang, F.; Ge, H.; Huang, Y. Quantitative Study on the Effect of Temperature on the Formation of Soil Desiccation Cracks in Red Soil Layer in Benggang Areas. *J. Soil Sci.* **2022**, *53*, 805–814. (In Chinese)
35. Ren, J.; Li, X.; Zhao, K.; Fu, B.; Tao, J. Study of an on-line measurement method for the salt parameters of soda-saline soils based on the texture features of cracks. *Geoderma* **2016**, *263*, 60–69. [[CrossRef](#)]
36. Yang, F.; Wang, Z.; Wang, Y.; An, F.; Yang, H. Soil water characteristics of saline-sodic soil in Songnen Plain. *Sci. Geogr. Sin.* **2015**, *35*, 340–345. (In Chinese)
37. Li, B.; Wang, Z.; Liang, Z.; Chi, C. Distribution characteristics of ions in sodic soil and correlation analysis. *Chin. J. Soil Sci.* **2007**, *38*, 653–656. (In Chinese)
38. Ren, J.; Xie, R.; Zhu, H.; Zhao, Y.; Zhang, Z. Comparative study on the abilities of different crack parameters to estimate the salinity of soda saline-alkali soil in Songnen Plain, China. *Catena* **2022**, *213*, 106221. [[CrossRef](#)]
39. Dhingra, S.; Bansal, P. Experimental analogy of different texture feature extraction techniques in image retrieval systems. *Multimed. Tools Appl.* **2020**, *79*, 27391–27406. [[CrossRef](#)]
40. Kushwaha, R.; Singal, G.; Nain, N. A texture feature based approach for person verification using footprint bio-metric. *Artif. Intell. Rev.* **2021**, *54*, 1581–1611. [[CrossRef](#)]
41. Lan, R.; Zhong, S.; Liu, Z.; Shi, Z.; Luo, X. A simple texture feature for retrieval of medical images. *Multimed. Tools Appl.* **2018**, *77*, 10853–10866. [[CrossRef](#)]
42. Aouat, S.; Ait-hammi, I.; Hamouchene, I. A new approach for texture segmentation based on the gray level co-occurrence matrix. *Multimed. Tools Appl.* **2021**, *80*, 24027–24052. [[CrossRef](#)]
43. Srivastava, D.; Rajitha, B.; Agarwal, S.; Singh, S. Pattern-based image retrieval using GLCM. *Neural Comput. Appl.* **2020**, *32*, 10819–10832. [[CrossRef](#)]
44. Haralick, R.M.; Shamugam, K.; Dinstein, I. Texture features for image classification. *IEEE Trans. Syst. Man Cybern.* **1973**, *3*, 610–621. [[CrossRef](#)]

45. Zhao, Y.; Zhang, Z.; Zhu, H.; Ren, J. Quantitative Response of Gray-Level Co-Occurrence Matrix Texture Features to the Salinity of Cracked Soda Saline–Alkali Soi. *Int. J. Environ. Res. Public Health* **2022**, *19*, 6555–6556.
46. Aneke, F.I.; Onyelowe, K.C.; Ebid, A.M.; Nwobia, L.I.; Adu, J.T. Predictive models of swelling stress—a comparative study between BP- and GRG-ANN. *Arab. J. Geosci.* **2022**, *15*, 1438. [[CrossRef](#)]
47. Cheng, X.; Hu, X.; Li, Z.; Geng, C.; Liu, J.; Liu, M.; Zhu, B.; Li, Q.; Chen, Q. Using genetic algorithm and particle swarm optimization BP neural network algorithm to improve marine oil spill prediction. *Water Air Soil Poll.* **2022**, *233*, 1–19. [[CrossRef](#)]
48. Panda, S.; Panda, G. Performance evaluation of a new BP algorithm for a modified artificial neural network. *Neural Process. Lett.* **2020**, *51*, 1869–1889. [[CrossRef](#)]
49. Adeloye, A.J.; Munari, A.D. Artificial neural network based generalized storage-yield-reliability models using the Levenberg-Marquardt algorithm. *J. Hydrol.* **2006**, *326*, 215–230. [[CrossRef](#)]
50. Zhou, Z.; Li, Z.; Zhang, Z.; You, L.; Xu, L.; Huang, H.; Wang, X.; Gao, Y.; Cui, X. Treatment of the saline-alkali soil with acidic corn stalk biochar and its effect on the sorghum yield in western Songnen Plain. *Sci. Total Environ.* **2021**, *797*, 149190. [[CrossRef](#)]
51. Zhang, X.; Huang, B.; Liang, Z.; Zhao, Y.; Sun, W.; Hu, W. Study on salinization characteristics of surface soil in western Songnen Plain. *Soils* **2013**, *45*, 332–338. (In Chinese)
52. Wang, L.; Yan, B.; Zhu, L.; Ou, Y. The effect of reclamation on the distribution of heavy metals in saline-sodic soil of Songnen Plain, China. *Environ. Earth Sci.* **2015**, *73*, 1083–1090. [[CrossRef](#)]
53. USSLS. *Diagnose and Improvement of Saline and Alkali Soils*; US Government Printing Office: Washington, DC, USA, 1954.
54. Li, X.; Cao, J.; Li, F. Influence of salinity, sodicity and organic matter on some physical properties of salt-affected soils. *Chin. J. Soil Sci.* **2004**, *35*, 64–72. (In Chinese)
55. Ren, J.; Li, X.; Zhao, K.; Zheng, X.; Jiang, T. Quantitative research on the relationship between salinity and crack length of soda saline-alkali soil. *Pol. J. Environ. Stud.* **2019**, *28*, 823–832. [[CrossRef](#)] [[PubMed](#)]
56. Zhang, Z.; Li, X.; Ren, J.; Zhou, S. Study on the drying process and the influencing factors of desiccation cracking of cohesive soda saline-alkali soil in the Songnen Plain, China. *Agriculture* **2023**, *13*, 1153. [[CrossRef](#)]
57. Rayhani, M.H.T.; Yanful, E.K.; Fakher, A. Physical modeling of desiccation cracking in plastic soils. *Eng. Geol.* **2008**, *97*, 25–31. [[CrossRef](#)]
58. Zhao, H.; Ma, Y.; Zhang, J.; Hu, Z.; Li, H.; Wang, Y.; Liu, J.; Li, Z. Effect of clay content on plastic shrinkage cracking of cementitious materials. *Constr. Build. Mater.* **2022**, *342*, 127989. [[CrossRef](#)]
59. Puppala, A.J.; Manosuthikij, T.; Chittoori, B.C.S. Swell and shrinkage characterizations of unsaturated expansive clays from Texas. *Eng. Geol.* **2013**, *164*, 187–194. [[CrossRef](#)]
60. Vail, M.; Zhu, C.; Tang, C.; Anderson, L.; Moroski, M.; Montalbo-Lomboy, M.T. Desiccation cracking behavior of MICP-treated bentonite. *Geosciences* **2019**, *9*, 385. [[CrossRef](#)]
61. Wang, W.; Wang, Q.; Zhang, J.; Chen, H. An Experiment Study of the Fundamental Property of the Carbonate-saline Soil in West of Jilin Province. *J. Beijing Univ. Technol.* **2011**, *37*, 217–224. (In Chinese)
62. Zhang, G.H.; Yu, Q.C.; Wei, G.Q.; Chen, B.; Yang, L.S.; Hu, C.Y.; Li, J.P.; Chen, H.H. Interpretation of salinity characteristics of normal profile in estuarine region by using electromagnetic induction. *Hydrogeol. Eng. Geol.* **2007**, *3*, 37–40. (In Chinese)
63. Zhang, G.; Li, J.; Yu, Q.; Zhang, B.; Chen, H. Effects of salinity on shear strength of saline alkali soils in Songnen plain. *Chin. J. Geol. Hazard Control* **2008**, *19*, 128–131.
64. Shokri, N.; Zhou, P.; Keshmiri, A. Patterns of desiccation cracks in saline bentonite layers. *Transport Porous Med.* **2015**, *110*, 333–344. [[CrossRef](#)]
65. Farifteh, J.; Van der Meer, F.; Atzberger, C.; Carranza, E.J.M. Quantitative analysis of salt-affected soil reflectance spectra: A comparison of two adaptive methods (PLSR and ANN). *Remote Sens. Environ.* **2007**, *110*, 59–78. [[CrossRef](#)]

Disclaimer/Publisher’s Note: The statements, opinions and data contained in all publications are solely those of the individual author(s) and contributor(s) and not of MDPI and/or the editor(s). MDPI and/or the editor(s) disclaim responsibility for any injury to people or property resulting from any ideas, methods, instructions or products referred to in the content.